MNRAS 000, 1–10 (2015) Preprint 3 August 2020 Compiled using MNRAS LATEX style file v3.0

Flares Big and Small: a K2 and TESS View of ASAS-SN Superflares

Jesse Zeldes[1,2], Jason T. Hinkle[1], Benjamin J. Shappee[1], Ellis A. Avallone[1], Jennifer L. van Saders[1], Sarah J. Schmidt[3], Krzysztof Z. Stanek[4,5], Zachary Way[4], Christopher S. Kochanek[4,5], Thomas W.-S. Holoien[6⋆], Subo Dong[7], Jose L. Prieto[8,9], and Todd A. Thompson[4,5]

[1]*Institute for Astronomy, University of Hawai'i, 2680 Woodlawn Dr., Honolulu, HI 96822, USA*
[2]*Haverford College, 370 Lancaster Ave., Haverford, PA, 19041, USA*
[3]*Leibniz-Institute for Astrophysics Potsdam (AIP), An der Sternwarte 16, D-14482, Potsdam, Germany*
[4]*Department of Astronomy, The Ohio State University, 140 West 18th Avenue, Columbus, OH 43210, USA*
[5]*Center for Cosmology and Astroparticle Physics, The Ohio State University, 191 W. Woodruff Avenue, Columbus, OH 43210, USA*
[6]*The Observatories of the Carnegie Institution for Science, 813 Santa Barbara St., Pasadena, CA 91101, USA*
[7]*Kavli Institute for Astronomy and Astrophysics, Peking University, Yi He Yuan Road 5, Hai Dian District, Beijing 100871, China*
[8]*Núcleo de Astronomía de la Facultad de Ingeniería y Ciencias, Universidad Diego Portales, Av. Ejército 441, Santiago, Chile*
[9]*Millennium Institute of Astrophysics, Santiago, Chile*

Accepted XXX. Received YYY; in original form ZZZ

ABSTRACT

We present an investigation of the flare-rate distributions of 5 M-dwarfs which experienced superflares with energy in excess of 10^{33} erg in the ASAS-SN data set. We use K2 and TESS short-cadence observations to categorize the regular flaring behavior of these stars at lower flare energies. Additionally, we extract a rotation period for 4 of the stars, and find each of them to be fast rotators ($P_{rot} \leq 10$d). We find that the flare frequency distributions for each of the stars in our sample follow a power law, with slope α in the range -1.22 to -1.78. These slopes are significantly flatter than those of populations of other fast-rotating M-dwarfs not selected for their superflaring activity.

Key words: stars: flare – stars: activity – stars: low-mass

1 INTRODUCTION

M-dwarfs (stars of effective temperature 2300K to 3800K) are some of the most magnetically active stars (Saar & Linsky 1985). This extreme magnetism manifests both through long term trends in magnetic activity and through more extreme events such as flares: sudden, multi-wavelength jumps in brightness caused by magnetic field lines reconnecting (Priest & Forbes 2002). These flares can provide a rare window into the underlying magnetic dynamics of these stars, which are otherwise hard to observe.

Understanding the flaring of these stars is also crucial to studies of exoplanet habitability (e.g., Grootel et al. 2018). Estimates hold that up to 70% of habitable zone planets orbit M-dwarfs (e.g., Dressing & Charbonneau 2015; Ilin et al. 2019), which make up ≈ 75% of main-sequence stars (e.g, Clements et al. 2017). Furthermore, due to their low luminosities, the habitable zones of M-dwarfs are very close to the star, often much less than 1AU (e.g., Luger & Barnes 2015). UV emission and ionized particles emitted during flares could deplete the atmospheres of planets in the M-dwarf's habitable zone, rendering them inhospitable (e.g., Khodachenko et al. 2007; Segura et al. 2010). This is particularly true of flares of the highest energies, which simulations suggest could be more damaging than equivalent magnetic energy released over time in smaller flares (e.g., Shields et al. 2016; Tilley et al. 2019).

Flares on M-dwarfs are thought to arise from similar mechanisms as those seen on the Sun and other solar-type stars (e.g., Hudson 1991; Hannah et al. 2011; Davenport et al. 2014). Ionized material circulating in the convective zone of a star leads to the emergence of a magnetic dynamo, a large scale magnetic structure that is relatively stable across large time scales (e.g., Priest & Forbes 2002; Browning 2008). As the fields slowly evolve, magnetic field lines will occasionally cross and reconnect, falling to a more stable configuration and releasing a burst of magnetic energy (e.g., Benz & Güdel 2010). This process accelerates charged particles in the star's upper atmosphere into the surface of the star, temporarily heating an area of the stellar surface to a temperature of about 10,000K (Kowalski et al. 2013). The radiation from this hot spot is then observed as a flare. Magnetic reconnection can also create beams of charged particles that are emitted outward from the star (Priest & Forbes 2002). M-dwarfs are intensely magnetic objects,

⋆ Carnegie Fellow

because their lower temperature creates convective zones that extend deep into the stellar interior (Hawley et al. 2014a). Because of this, flares on M-dwarfs are often much more energetic than those on the Sun, both in equivalent duration (ED) – a measure of how long in quiescence it would take a star to emit the energy of a flare – and occasionally in absolute magnitude (Davenport et al. 2014).

Flares typically consist of three parts: a rapid, quartic polynomial rise toward the maximum flux, an initial decay phase that lasts on the scale of minutes, and a secondary exponential decay that lasts on the scale of hours (Davenport et al. 2014). The length of a flare scales roughly linearly with the peak flux during the flare (Hawley et al. 2014b), though the relationship is different for simple flares that consist of a single peak, and complex multi-peaked flares (Silverberg et al. 2016). Flaring M-dwarfs typically flare stochastically and frequently, often multiple times per day, with most flares being concentrated at lower energies (e.g., Hawley et al. 2014a; West & Hawley 2008; Paudel et al. 2018). The exact relationship between flare energy and frequency has been a subject of intense study. This relationship is typically quantified through the flare frequency distribution (FFD), a comparison of the frequencies of flares of different energies. FFDs are thought to follow a power law distribution (e.g Gershburg & Shakahovskaya 1973; Lacy et al. 1976a; Günther et al. 2020) of the form $f = \beta(E/E_{\rm base})^{-\alpha}$, where f is the frequency in flares per day, E is the flare energy, and $E_{\rm base}$ is the baseline energy around which the power law is fit.

Some M-type dwarfs have also been observed to undergo superflaring, defined as flares of energy in excess of 10^{33} erg, which often manifest as an increase in brightness of 3 magnitudes or more (Maehara et al. 2012). Paudel et al. (2019) suggest that these types of flares could appear most often on young, fast-rotating stars due to the rotation fueling a more powerful magnetic dynamo. However, these results are in tension with other studies, such as Mondrik et al. (2018), who find lower flaring rates in fast rotating (period < 10d) stars than in those with intermediate (10 – 70d) rotation periods.

Along with driving stellar dynamos, rotation is also a useful tool for determining M-dwarf ages (Barnes 2003, 2007). Gyrochronology utilizes the observation that stars spin down as they age to estimate ages of stars with known rotation periods (e.g. Skumanich 1972). This technique is especially useful for M-dwarfs, where techniques such as isochrone fitting are inconclusive due to M-dwarfs' long main-sequence lifetimes.

The stochastic nature of flares has presented challenges for traditional ground-based observing campaigns (Lacy et al. 1976a). Even resource-intensive, multi-night monitoring campaigns may only yield a few dozen flare light curves per star, and often none of the highest energies (Hilton 2011). Space-based observation provides an attractive alternative; missions like Kepler and TESS have much longer continuous baseline observations for each star, opening the door for in depth studies of flaring behavior. The Kepler Space Telescope was an exoplanet finding mission, which monitored 200,000 stars looking for planetary transits (Borucki et al. 2010). Kepler, and its follow-up mission K2, (Howell et al. 2014) have proved crucial tools for studying flares (e.g. Hawley et al. 2014a; Davenport et al. 2014; Mondrik et al. 2018; Gizis et al. 2017). Constant white light monitoring of targets has enabled reliable measurements of flares across the energy spectrum. In its one-minute short cadence mode, K2 can obtain multiple data points for even short, low-energy flares. Studies such as Notsu et al. (2013), Paudel et al. (2019), and Ilin et al. (2019) have taken advantage of this to explore the energy distributions of flares in K2 data, allowing for the first complete classifications of the flaring behavior of stars other than the Sun.

The successor mission to K2, the Transiting Exoplanet Survey Satellite (TESS, Ricker et al. 2014) has also proved a valuable tool for observing M-dwarf flares (e.g., Günther et al. 2020; Davenport et al. 2020). Unlike Kepler, which focused on finding planets around Sun-like stars, TESS's primary science mission seeks to observe planetary transits around low-mass dwarfs. To date, TESS has observed over 200,000 stars in its 2 minute short cadence mode, many of which seem promising targets for flare finding missions.

While the long baseline and fine precision of space telescopes are unparalleled for single target flare investigations, automated ground-based surveys are useful for flare categorization in their ability to search for flares across many more targets simultaneously (e.g., Kowalski et al. 2009; Hilton et al. 2010; Gizis et al. 2013). The All-Sky Automated Survey for Supernovae (ASAS-SN, Shappee et al. 2014; Kochanek et al. 2017) monitors the entire sky to a depth of $g, V \approx 18$ mag with a cadence of ~ 1 day, with a goal of detecting all visible nearby supernovae. The regular cadence and large search area have enabled ASAS-SN to discover many large flares from L- and M-type dwarfs (Stanek et al. 2013; Schmidt et al. 2014; Simonian et al. 2016). A detailed treatment of M-dwarf flares detected in ASAS-SN V-band data can be found in Schmidt et al. (2019) and (Martínez et al. 2020).

ASAS-SN data has allowed for a better understanding of the frequency of superflares and the stars they originate on, but is only able to detect the flares with the highest energies. This makes it difficult to categorize the properties of the stars on which the flares are observed. In this paper, we use K2 and TESS short cadence observations to examine examine 5 M-dwarfs observed superflaring in ASAS-SN. The details of the ASAS-SN, K2 and TESS data are described in Section 2. In Section 3, we attempt to extract a rotation rate of each of the stars, and use this to get an estimate the star's age. In Section 4, we look at the flare frequency distribution of each of the stars. Section 5 provides a discussion of the results.

2 METHODS

In this section, we outline our procedure for finding candidate flare stars, finding flares in their K2 and TESS light curves, and recovering frequencies and bolometric energies for these events. Section 2.1 describes the data from the ASAS-SN survey and our target selection criteria. In Section 2.2 we outline our processing and detrending of our space telescope data. In Section 2.3, we explain our flare finding algorithm and introduce `AltaiPony`, a python based package for automated flare finding. Section 2.4 outlines our procedure for extracting bolometric energies from identified flares. Finally, in Section 2.5, we explain our injection and recovery process, which is used to make a final correction to flare energies and frequencies.

2.1 ASAS-SN Pipeline and Sample Selection

The ASAS-SN survey is the first project to monitor the entire sky for transients with a regular cadence. Since beginning to search for real-time transients in April 2013, ASAS-SN has undergone a number of expansions, including building additional robotic telescopes at sites in Chile, South Africa and Texas (Holoien et al. 2017; Kochanek et al. 2017). These telescopes, along with the two original instruments at sites in Hawaii and Chile, allow the ASAS-SN project to monitor the entire sky to a depth of $g \approx 18.5$ mag approximately every 20 hours (Schmidt et al. 2019). The superflares that motivated this study, with the exception of the flare on ASASSN-20gu, were

each observed when the ASAS-SN project still consisted of two telescopes, which monitored the sky to a depth of $V \approx 16.5$ mag - 17.3 mag, depending on conditions. For each of the stars in our sample, we search the ASAS-SN g-band data for additional flare candidates.

For this paper, we consider any star which was observed to flare in ASAS-SN with a recovered energy greater than 10^{33} erg (as estimated by Schmidt et al. 2019), that was also observed in short-cadence mode by either TESS or K2 for at least one sector or quarter, respectively. This gave us a total of 4 candidate stars, the M4 dwarfs ASASSN-13cm, -14jy, and -16dj, each observed in TESS, and the M6 dwarf ASASSN-14mz, which we observed in K2. We also examine the M3 dwarf ASASSN-20gu, which was recently observed flaring by ASAS-SN in the g-band and for which TESS short cadence data was available. Table 1 gives the observational details for each of the targets, along with stellar properties.

2.2 K2 and TESS Pipeline

We obtained K2 data for ASASSN-14mz through the K2 guest observer program[1]. Detrending of K2 light curves was done using `K2SC` (Aigrain et al. 2016), which allows the removal of K2 systematics to almost the level of precision of the original Kepler mission. `K2SC` uses Gaussian processes to model the telescope pointing jitter introduced by K2's periodic corrections using the solar wind. It uses correlations across pixels in the K2 field to correct for position-dependent systematics while maintaining time-dependent variability. We split the lightcurve into 4 sections, using the recommended `K2SC` splits, then detrend each separately.

For our TESS analysis, we use the `PDCSAP FLUX` lightcurves, which we obtain directly from the TESS mission. We require the `quality` flag to be set to 0, to insure the highest fidelity light curves. TESS data are detrended using a 3rd order Savitzky–Golay filter, implementing the sigma clipping approach described in Davenport (2016). This enables the smoothing of the data to remove small scale systematics with little loss to true variability.

2.3 Flare Identification

The detrending and flare finding algorithms are implemented through `AltaiPony`[2], a python based package for the analysis of Flares in Kepler, K2 and TESS data. `AltaiPony` (E. Ilin et al., 2020 in preparation) was developed by E. Ilin as a successor to the flare finding software `appaloosa` (Davenport 2016). AltaiPony enables the user to directly download, detrend, and find flares in both short- and long-cadence Kepler, K2, and TESS lightcurves. Both the K2 and TESS detrending procedures are implemented through the `FlareLightCurve Detrend` method.

We found a preliminary sample of flare candidates using the `AltaiPony find_flares` method, which implements the `FINDflare` algorithm defined in Chang et al. (2015). For an event x_i at the ith position of a light curve segment L to be categorized as a candidate flare, we require that it pass 3 criteria N_1 , N_2 and N_3, where

$$\frac{|x_{\rm i} - \bar{x}_{\rm L}|}{\sigma_{\rm L}} \geq N_1 \tag{1}$$

[1] Investigation ID: GO16104_SC
[2] https://github.com/ekaterinailin/AltaiPony/

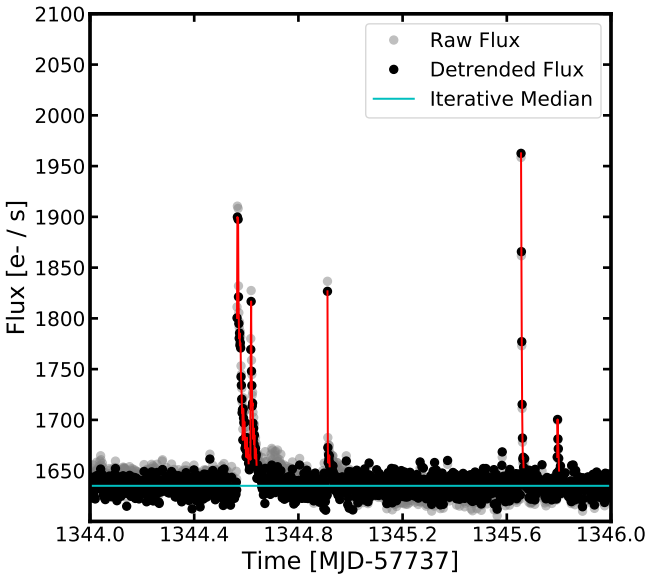

Figure 1. An example of a 2-day portion of a lightcurve for one of our targets, the TESS star ASASSN-14jy. The raw flux is in grey, while the detrended flux is in black. The flares detected by our FINDflare algorithm are highlighted in red. The flares occur stochastically across the light curve, and span a range of energies.

where $\bar{x}_L$ is the mean of the local segment, and σ_L is the standard deviation. To account for photometric uncertainty we also require

$$\frac{|x_{\rm i} - \bar{x}_{\rm L} + \omega_{\rm i}|}{\sigma_{\rm L}} \geq N_2 \tag{2}$$

where ω_i is the photometric uncertainty at position i. Finally, we require that

$$N_{dat} \geq N_3. \tag{3}$$

where N_{dat} is the number of data points in the candidate flare. We choose $N_3 = 4$ for our 1-minute K2 data and $N_3 = 2$ for our 2-minute TESS data, yielding a minimum detectable flare length of 4 minutes for both TESS and K2. For both data sets, we choose $N_1 = 3, N_2 = 4$, as consistent with Ilin et al. (2019). We test a number of other parameter configurations, and find that these are best able to effectively recover most of the events that appear to be flares by eye, while minimizing false positives due to instrumental variability.

Figure 1 shows a portion of TESS data for the target ASASSN-14jy. The `FINDflare` algorithm identified 5 flares over an approximately 2-day section of data. The flares, highlighted in red, span a range of energies. Other events, where only a single elevated point is visible, are not categorized as flares. Though it is possible that these points do originate from true magnetic variability on the star, the lack of temporal resolution makes it impossible to identify the classic flare shape and disambiguate these points from other kinds of background noise.

An example flare identified by the `FINDflare` algorithm for the K2 target ASASSN-14mz is shown in Figure 2. The characteristic shape of the flare, consisting of an impulsive rise followed by an exponential decay, is clearly evident in the data. This flare has an

Target	Stellar Type	Energy (log erg)	Observation	Quarter / Sector	RA	Dec	Distance (pc)
ASASSN-13cm	M4	33.49	TESS	3	01 46 51.4	-16 52 19.7	59.1 ± 0.2
ASASSN-14jy	M4	34.21	TESS	1-4, 6-13	07 06 58.9	-62 21 10.9	46.3 ± 0.1
ASASSN-14mz	M6	33.84	K2	16	08 51 13.9	+19 12 21.5	74.4 ± 13.5
ASASSN-16dj	M4	33.92	TESS	14, 20, 21	10 07 17.7	+69 20 46.2	52.5 ± 0.1
ASASSN-20gu	M3		TESS	14	19 35 29.05	+37 46 06.2	14.4 ± 0.01

Table 1. The observation properties of each M-dwarf. The energy of the the triggering superflare in ASAS-SN is estimated using the template fit described in Schmidt et al. (2019).

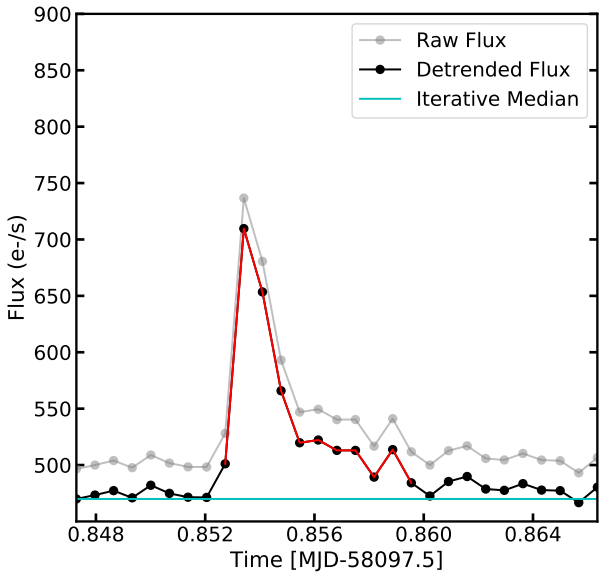

Figure 2. An example flare classified in our data for the K2 target ASASSN-14mz. The raw flux is shown in grey, while the detrended flux is in black. The red outline shows the points that the `FINDFlare` algorithm classified as part of the event.

approximate duration of 8 minutes, and an uncorrected ED of 92.5s. Note that it is not entirely clear at which points the flare begins and ends, and that the area before the first point of the rise is not counted as part of the flare. Correcting for these variations in identified points is an important part of the injection and recovery process.

2.4 Flare Energy Estimate

In order to accurately measure the energy released during flares, an accurate estimate of distance is needed. For each of the TESS targets, ASASSN-13cm, -14jy, -16dj and -16gt, we use parallax data from Gaia to obtain a distance estimate (Gaia Collaboration et al. 2018). Due to the presence of nearby background objects, reliable parallax data was not available for ASASSN-14mz in Gaia. We use the distance value computed in Schmidt et al. (2019), derived from the $V - K_s$ relation from (Henry et al. 2004). Estimated distances for each target are given in Table 1.

Once we have the distance and flux measurements throughout the lifetime of the flare, we are able to recover a flare energy. First, we recover the ED of the event in the Kepler or TESS band. This is given by the area between the light curve and the quiescent flux (Hunt-Walker et al. 2012), divided by the quiescent flux. Typical values can range from 5s for relatively small flares, to over 6000s for the largest flares in our sample. The bolometric energy of the flare is therefore given by

$$E_{\rm bol} = \frac{1}{c_{\rm band}} L_{\rm band} E D \tag{4}$$

where $L_{\rm band}$ is the luminosity in the TESS or Kepler band and $c_{\rm band}$ is the fraction of the bolometric luminosity that lies in the band. Following Paudel et al. (2019) and measurements from Kowalski et al. (2013), we assume the flares to have the spectrum of a 10,000K blackbody. We then convolve the blackbody spectrum with the filter and integrate. We compute this value to be approximately 0.209 for Kepler and 0.178 for TESS. This approximation underestimates the energy in each flare, due to the loss of flux from emission lines outside the Kepler band (Kowalski et al. 2013), but the error is small, as the blackbody continuum dominates the flare energy budget in UV/visible wavelengths (e.g., Hawley & Pettersen 1991; Osten & Wolk 2015; Paudel et al. 2019). Then, we make one final correction to the energy through our injection and recovery process.

2.5 Injection and Recovery

Injection and recovery analysis serves two purposes: (1) it quantifies how flare finding efficiency drops off at low energy levels, and (2) we use it to correct the systematic under-recovery of injected EDs due to energy removed by the detrending process and insufficiently fine sampling cadence. For each star, we inject 50,000 flares over many iterations, ensuring that injected flares are spaced apart by at least 4x the length of the previous flare, and that they do not overlap with flares already in the data. The injected flare EDs are sampled from a power law given by a preliminary fit to the ED-frequency relation, with an additional Gaussian noise component. The template for each of the injected flares in generated using `AltaiPony`'s `sample_flare_recovery` method, which generates the flares based on the template given in Davenport et al. (2014), with the addition of Gaussian noise. For TESS targets, we run our detrending procedure after injection before running our standard `FINDflare` recovery procedure, though this was not possible for our K2 target due to computational limitations. For stars with light curves from multiple sectors, we run the process separately on each sector to account for differing systematics. A flare was considered recovered if the flare peak time was contained within the start and end times of any resulting flare event candidate.

A primary weakness of this method is that it assumes that all flares follow the same basic template. This template is built from data from a single star, the M4 dwarf GJ 1243, so if flares on other stars are generated by a different mechanism may not be applicable. Additionally, when developing the template, Davenport

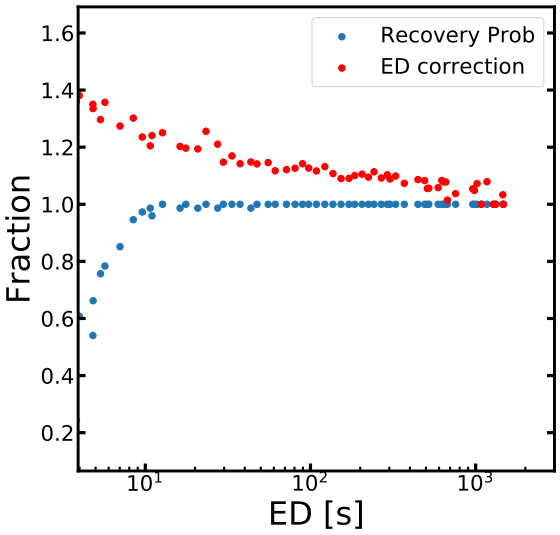

Figure 3. Recovery probability and ED correction for the recovery process as a function of the flares' injected ED for the target ASASSN-14jy. Each bin contains approximately 100 flares. Recovery probability is very close to 1 for all EDs greater than 100s, meaning we recover nearly all flares above this threshold.

et al. (2014) found that ≈ 15% of flares were "complex" events, which are not well fit by the example template, and that complex events are more common at higher energies. As flare recovery rates approach 100% at higher energies, regardless of flare shape, these high energy differences become less important. Nevertheless, our injection and recovery method is likely good to a 15% level, and does an improved job correcting at lower energies where it is most important.

After recovery, the injected flares are separated into 100 bins by log ED. For each bin, we calculate the recovery probability, as well as the ratio of injected to recovered ED. Figure 3 shows a plot of recovery probability and ED correction as a function of ED for the K2 target ASASSN-14mz. For all flares with ED> 30s, the recovery probability is greater than 0.5, and it approaches 1 around an ED of 100s. There is typically a small ED correction, between 1 and 1.2 for most flare energies less than 1000s. This recovery probability and ED correction are then used to correct the energies of the detected flares. We multiply each flare's recovered ED by the ED correction to derive an estimated flare energy. We then multiply each frequency by the inverse of the recovery probability. We propagate any relevant errors, including Poisson error from the number of simulated flares in each bin.

3 ROTATION ANALYSIS

We measured rotation periods for our stars using Fourier analysis, wavelet analysis, and autocorrelation function (ACF) analysis. Previous work has shown that using these methods together with one another optimizes the recovery of stellar rotation periods (Ceillier et al. 2017).

Fourier analysis utilizes Fourier transforms to recover periodic trends found in timeseries data. Lomb-Scargle periodograms build upon Fourier analysis by showing which recovered periods have the strongest power. We utilize the Lomb-Scargle periodogram method within the lightcurve processing package `lightkurve` (Lightkurve Collaboration et al. 2018) to compute periodograms for each of our stars. For TESS lightcurves, we remove peaks in the periodogram that are within 0.1 days of TESS aliases at 14, 27, 90, and 120 days. We then recompute the periodogram with finer sampling around the highest peak in the initial periodogram. We use the largest peak in the zoomed-in periodogram as our final Fourier analysis rotation period.

Fourier analysis, however, falls short by focusing on purely periodic phenomena. Starspots are transient features on a star's surface, and often appear as a mixture of periodic and aperiodic signals in the lightcurve. Wavelet analysis overcomes this by recovering periods present in a slice of timeseries data and stepping through the rest of the time series to validate those recovered periods. We used the wavelet transform and the Morlet wavelet in the `SciPy` library to perform these measurements (Virtanen et al. 2020). As with Lomb-Scargle periodograms, we first compute the wavelet power spectrum and global wavelet power spectrum (GWPS), which is equal to the wavelet power spectrum summed over the full timeseries, with coarse spacing in frequency. We remove any peaks that correspond to TESS aliases, then zoom in on the region in the GWPS around the largest peak and compute the wavelet power spectrum and the GWPS with finer sampling. Our final rotation period from wavelet analysis is given by the highest peak in the zoomed-in GWPS.

ACF analysis searches for periodic signals by correlating timeseries data with itself at multiple points along the timeseries. This method confirms signals found through Fourier and wavelet analysis while also searching for signals that are not perfectly periodic, sinusoidally shaped, or present throughout the full lightcurve. We use the methods outlined in McQuillan et al. (2013) and the Python package `starspot`[3] to compute rotation periods with ACF analysis. As with Fourier and wavelet analysis, for TESS lightcurves, we ignore any peaks in the ACF that correspond to TESS aliases. Our final rotation period from ACF analysis is equal to the first peak or the second peak in the ACF if the second peak is larger than the first peak.

We compute the uncertainty on our measured rotation periods following several methods. First, there is a fundamental limit on the precision of any measured rotation period of 10% due to differential rotation, as described in Epstein & Pinsonneault (2014). The statistical uncertainty for each of our methods is derived from the width of the peak corresponding to the rotation period in the zoomed-in Lomb-Scargle periodogram, zoomed-in GWPS, and ACF. We propagate the systematic uncertainty from Epstein & Pinsonneault (2014) with the statistical uncertainty from each of our rotation period measurement methods to obtain the final uncertainty on the photometric rotation period for each star.

Figure 4 shows an example of our rotation finding methods applied to the TESS target 14jy. All three methods agree to within 10 %, indicating a clear rotation signal at ≈ 5.25 days. The rotation periods for each of our targets are given in Table 2. For each of the stars that we were able to extract a rotation rate, we found them to be fast rotators, with a period less than 10 days, but more than 1 day. This lies in the range that studies such as Mondrik et al. (2018) and Raetz, St. et al. (2020) have found to be the most active in flaring behavior. It is also in line with theoretical predictions, which expect high superflaring rate at intermediate Rossby number.

[3] https://github.com/RuthAngus/starspot

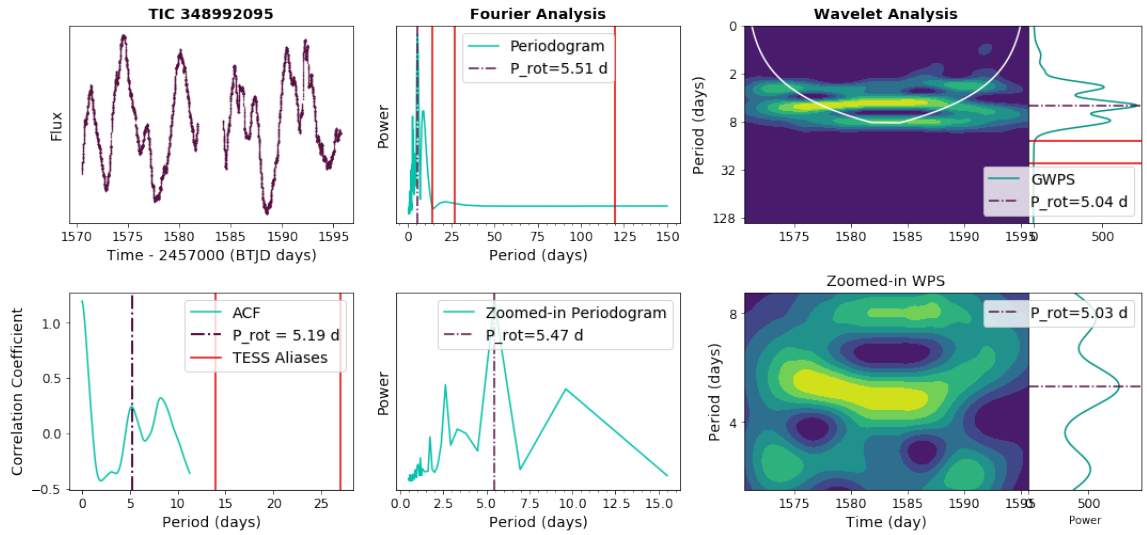

Figure 4. Our rotation analysis for ASASSN-14jy. The full, detrended lightcurve with flares removed is in the top left panel. The bottom leftmost panel shows the results of the ACF analysis, where a correlation peak its visible at 5.19 days. The middle panels give the Lomb-Scargle periodogram, while the right panels shows the results of Wavelet analysis. A full description of each method is given in 3. All three methods for rotation rate extraction find a peak in power at about ≈ 5 days. The power peaks are clear, and consistent at the 10% level, evidence of a clear rotation signal present.

4 FLARE DISTRIBUTION

We analyze the statistical flaring properties of each of our stars using a flare frequency distribution. Figure 5 shows the cumulative FFDs for each of our targets in ED. We compute the cumulative flare frequency for a given flare by counting the number of flares with energy greater than or equal to that flare, and dividing by the stars total observation time (defined as the total number of good points multiplied by the observing cadence, Gizis et al. 2013). The error bars on ED are given by uncertainty in the ED correction for each star, which arises because observing cadence can overlap with the flare shape in a variety of ways, giving different energy measurements. Power law fits are shown for each of the stars, the details of which are described in 4.0.1.

We also introduce a binned FFD, which allows us to correct directly for our flare detection probability. While previous studies such as Ilin et al. (2019) have computed detection probabilities, they have used them as a cutoff, discarding flares with a detection probability below a certain threshold, as opposed to correcting for them directly. Working with a binned distribution allows us to avoid this problem. A binned distribution also allows us to measure errors in frequency that are not covariant between flares.

For our binned distribution, we separate the flares into bins of equal size in log energy, choosing the number of bins to minimize uncertainty on the final fit. We then divide by the bin width, to normalize for the different bin sizes when not in log space. The frequency of flares in each bin is given by the number of flares in the bin, divided by the total observing time during which those flares could have been observed. Figure 6 gives the binned flare frequency distributions for each of our targets. The x error bars show the full with of the bin in which the frequency was computed and the central point shows the median flare energy in that bin. The error bars on the frequency are derived from a combination of Poisson error in the bin with uncertainty on our recovery probability from our injection and recovery process.

4.0.1 *Power Law Fitting*

From the earliest studies of flare distributions (Gershburg & Shakhovskaya 1973; Lacy et al. 1976b), the energy distributions of flares have been described by power laws. The spectral index $-\alpha$, has important implications for a number of stellar properties. To fit our power law, we work with our binned FFD. We use the median flare energy in each bin as our x value in that bin. We take the log of the medians and the frequencies, then fit a linear function to the log data using a `SciPy optimize` least squares optimizer. We choose $E_{\rm base} = 10^{31}$erg, so β represents the flaring rate at 10^{31} erg (in units of flares per day per erg). Fitting our data in this manner gives a direct measurement of the slope of the binned distribution, while the slope of the cumulative distribution is given by $\alpha' = \alpha - 1$ (Paudel et al. 2018). Parameters of the power law fit for each target are given in Table 2. We estimate the two sided error bars on our power law fitting using bootstrapping methods. For each star, we sample N flares with replacement from the original flare distribution, where N is the number of flares in the original distribution. We then run our full binning and power law fitting routine on this new distribution, computing values for α and β. We do this 1000 times, and report our two sided error bars as the 16th and 84th percentile of the distributions of α and β.

4.1 Estimating flare frequency in ASAS-SN

While the K2 and TESS data provide the most comprehensive view of the flares on each of our targets, the longer baseline of ASAS-SN is also useful for providing constrains on the highest energy flares. Due to the differences in observation style and completeness, we do not directly include ASAS-SN flares in our FFDs, instead, we provide a brief discussion of the ASAS-SN flaring behavior of each star. Beyond the superflare that was the selection criteria for this work, we observe an additional 8 flares on ASASSN-14jy, 5 additional flares on ASASSN-20gu, 4 additional flares on ASASSN-13cm, 2 additional flares on ASASSN-16dj, and no additional flares on ASASSN-14mz.

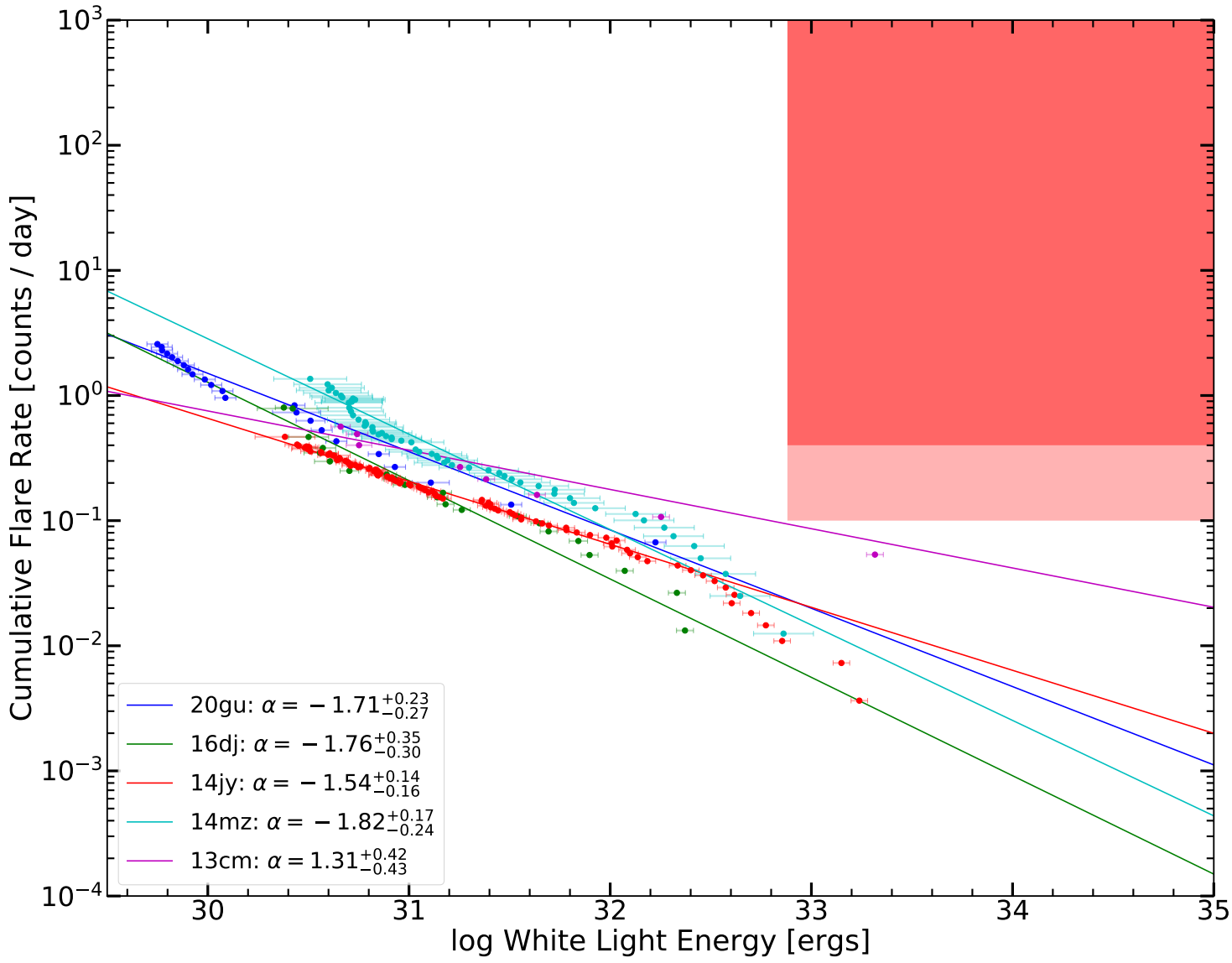

Figure 5. Cumulative FFDs for each of our stars. Error bars on energy come from a combination of distance uncertainty with the uncertainty in ED correction in our injection and recovery analysis. The fits shown are obtained from the best fit slope in the binned distribution. The red area denotes the ozone depletion zone, where there is sufficient UV flux in flares to deplete the atmosphere of a earth-like planet orbiting in the habitually zone of the star. The two color gradients denote the permissive and conservative thresholds given in Günther et al. (2020). None of our stars' FFDs intersect with this region.

The typical ASAS-SN observation strategy observes 2 to 3 90-second dithers on a section of sky before moving on to a new field. This does not provide enough data points for a detailed analysis of the lightcurve, as is possible in K2 and TESS data, but it does allow us to place a lower limit on flare energy. We calculate an estimated minimum energy by fitting a flare using the template from Davenport et al. (2014). We assume that the flare peak occurred during the ASAS-SN observations, and that the characteristic time scale $t_{1/2}$ is within the range 10s $\leq t_{1/2} \leq$ 2000s. We make a grid of possible distributions of $t_{1/2}$ and peak location, then integrate each over 90 second intervals. We consider each combination of $t_{1/2}$ and peak location that agrees with each of our observed ASAS-SN data points to be a possible flare parameterization, and compute the energy of each. We then report the median of these energies to be our most likely energy, and the 1st and 3rd quartiles to be our asymmetric error bars. Estimated ASAS-SN g-band flare energies are given in Table 2.

5 DISCUSSION

The FFD slope parameter α plays an important role in the physics of stellar coronae. Doyle et al. (1990) first proposed flares as a coronal heating mechanism. Güdel (2004) found that sufficient energy required to power coronal heating could be provided by many low energy microflares. If the distribution of flares were sufficiently steep, with $\alpha > 2$, then there could be enough power provided from low energy flares to fully heat the corona. Ilin et al. (2019) found that for a sample of stars in open clusters observed using K2 short cadence data, all of them had $2 \leq \alpha \leq 2.4$, suggesting that the coronae on young M-dwarfs could be primarily flare powered. Our

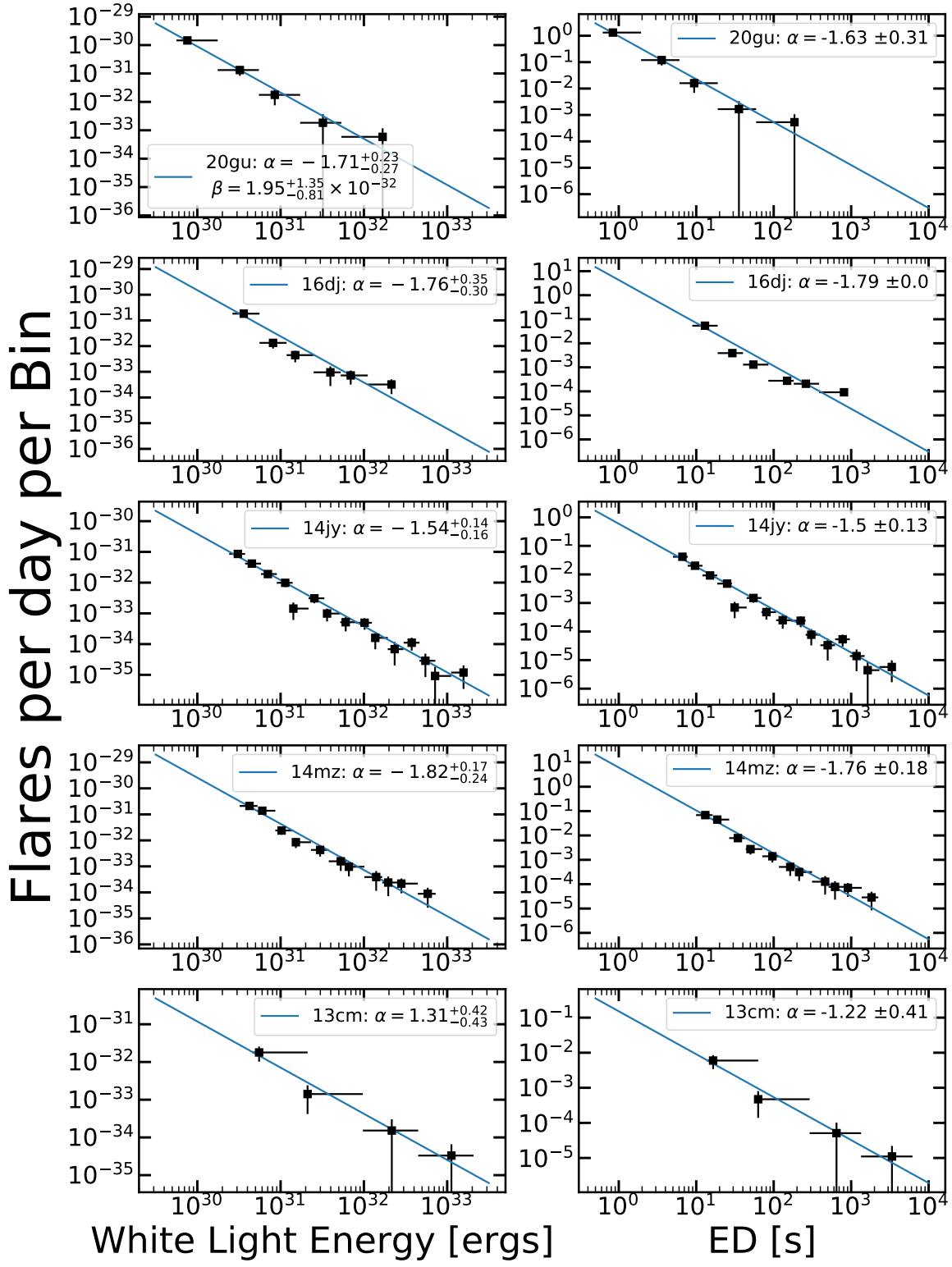

Figure 6. A binned FFD for each of our stars. We plot in energy per bin so that the best fit slope is not dependent on the number of bins. The x error bars show the full width of each bin. A point is places at the median ED value in each bin. We fit a power law to each of the FFDs as described in 4.0.1. We find each of the slopes to be < 2. The rate r is the estimated number of flares with white light energy greater than 10^{31} erg per day.

Target	Periodogram Rotation Period (days)	Number of Flares (TESS/K2, ASAS-SN g-band)	α	β (flares/day/erg)	Flare Rate (flares/day)	ASAS-SN g-band Flare Energies
ASASSN-13cm	1.20	8 , 4	1.22 ±	$7.09 * 10^{-31}$	0.316	
ASASSN-14jy	5.47	97 , 8	1.50 ±	$1.21 * 10^{-31}$	0.557	
ASASSN-14mz	N/A	58 , 0	1.78 ±	$4.31 * 10^{-31}$	0.241	
ASASSN-16dj	1.20	21 , 2	1.80 ±	$2.39 * 10^{-31}$	0.300	
ASASSN-20gu	5.48	23 , 5	1.63 ±	$2.12 * 10^{-31}$	0.281	

Table 2. The essential FFD parameters for each of our targets. Flare rate is the rate of flares with white light energy greater than 10^{31} erg. It is estimated assuming a power law fit and integrating, as opposed to directly counting flares. Much of the info in this table still needs to be finalized and filled in, but this is what the final version will look like.

results are in tension with these. Within 1σ error bars, we find that 3 of our targets have a Flare Frequency distribution with $\alpha \leq 2$, suggesting that flares are unlikely the source of a coronal heating mechanism on these stars.

There is significant heterogeneity in the literature both in power law fitting methods and injection and recovery techniques. Most of the literature fits directly to the cumulative flare distribution through a maximum likelihood estimator (e.g. Ilin et al. 2019), though some studies, such as Hawley et al. (2014a), have fit to a binned distribution. To confirm that our flatter slopes are not the result of fitting method, we fit each of our cumulative distributions using the maximum likelihood based `fit_power_law` method in `AltaiPony`. We find that each cumulative FFD power law fit still has $\alpha < 2$. Additionally, our investigation uses injection and recovery methods, while some previous studies do not. Typically, the injection and recovery process makes the recovered power law slope steeper, because it corrects for the many low energy flares that are missed. So, our use of injection and recovery is unlikely to be the source of our unusually flat FFD slopes.

Large flares can also impact the atmospheres of exoplanets orbiting M-dwarfs. The largest superflares on M-dwarfs are often orders of magnitude larger than the largest solar flare recorded, the Carrington Event of 1859. This, combined with the fact that the habitable zone of M-dwarfs is much smaller than 1 AU, means that possible life-bearing planets orbiting M-dwarfs could experience temporary UV fluxes 4 or more orders of magnitude larger than those which regularly strike the Earth. Tilley et al. (2019) estimate the rate of superflaring with $E \geq 10^{34}$erg needed to fully deplete the ozone layer of an earth-like planet in the habitable zone of a mid M-dwarf to be approximately .4 flares / day. In their analysis of flaring M-dwarfs in the first two sectors of TESS, Günther et al. (2020) offer the more permissive threshold of .1 flares / day. Figure 5 denotes the region of ozone depletion in red. Each of our targets fall below the region, though ASASSN-13cm has a relatively high superflare frequency of 0.064 flares / day. So, even on our targets with significantly flatter FFDs that were selected for superflaring activity, ozone depletion from direct UV emission is unlikely. This aligns with the results of Günther et al. (2020), who found only 15 M-dwarfs in the oxygen depletion region out of a sample of 1228 flaring stars.

6 SUMMARY

We analyze the flare distributions of 5 M-dwarfs which were observed undergoing a superflare in ASAS-SN, as well as by K2 or TESS short cadence for at least one sector. We use the `FINDflare` algorithm, implemented through `AltaiPony`, to identify flares in the detrended K2 and TESS data. We identity 207 flares across our light curves, as well as an additional 19 flares in ASAS-SN g-band data. We run injection and recovery routines for each of our stars, and derive ED correction and recovery probabilities for each of the flares in our sample. Additionally, we extract rotation rates for 4 of our targets, and find each of them to be fast-rotating, with $P < 10$ days. This lends evidence to the theory that superflares are more likely on faster rotating, more magnetically active stars.

We present the cumulative FFDs for each star. We also introduce a binned FFD, which allows us to directly correct for recovery probability, and to remove covariences between the frequency errors of points. Fitting a power law to each of the flare distributions, we find that each of them has $\alpha < 2$. We also calculate a flare rate for each star. Our results suggest that stars selected for their superflaring activity have $\alpha < 2$, lending evidence against the hypothesis that most M-dwarfs, regardless of properties, have $\alpha \approx 2$.

Short cadence K2 and TESS data in conjunction with effective automated flare finding techniques have made possible a broader understanding of flaring on low mass dwarfs. These new data enable studies of the statistics of flare distributions across a much larger sample of stars, which can be particularly helpful in deciphering the underlying physical mechanisms behind flares.

ACKNOWLEDGEMENTS

We thank Nicholas Saunders and Ekaterina Ilin for helpful discussions.

JZ acknowledges support from Research Experience for Undergraduate program at the Institute for Astronomy, University of Hawaii-Manoa funded through NSF grant 6104374. JZ would also like to thank the Institute for Astronomy for their kind hospitality during the course of this project.

We thank the Las Cumbres Observatory and its staff for its continuing support of the ASAS-SN project. ASAS-SN is supported by the Gordon and Betty Moore Foundation through grant GBMF5490 to the Ohio State University, and NSF grants AST-1515927 and AST-1908570. Development of ASAS-SN has been supported by NSF grant AST-0908816, the Mt. Cuba Astronomical Foundation, the Center for Cosmology and AstroParticle Physics at the Ohio State University, the Chinese Academy of Sciences South America Center for Astronomy (CAS- SACA), and the Villum Foundation.

BJS, CSK, and KZS are supported by NSF grant AST-1907570. BJS is also supported by NASA grant 80NSSC19K1717 and NSF grants AST-1920392 and AST-1911074. CSK and KZS are supported by NSF grant AST-181440. MAT acknowledges support from the DOE CSGF through grant DE-SC0019323. Support for JLP is provided in part by FONDECYT through the grant 1151445

and by the Ministry of Economy, Development, and Tourism's Millennium Science Initiative through grant IC120009, awarded to The Millennium Institute of Astrophysics, MAS. TAT is supported in part by Scialog Scholar grant 24215 from the Research Corporation.

Parts of this research were supported by the Australian Research Council Centre of Excellence for All Sky Astrophysics in 3 Dimensions (ASTRO 3D), through project number CE170100013.

This work is based on observations made by ASAS-SN. We wish to extend our special thanks to those of Hawaiian ancestry on whose sacred mountain of Maunakea we are privileged to be guests. Without their generous hospitality, the observations presented herein wouldnot have been possible.

REFERENCES

Aigrain S., Parviainen H., Pope B. J. S., 2016, MNRAS, 459, 2408
Barnes S. A., 2003, ApJ, 586, 464
Barnes S. A., 2007, ApJ, 669, 1167
Benz A., Güdel M., 2010, Annual Review of Astronomy and Astrophysics, 48, 241
Borucki W. J., et al., 2010, Science, 327, 977
Browning M. K., 2008, ApJ, 676, 1262
Ceillier T., et al., 2017, A&A, 605, A111
Chang S. W., Byun Y. I., Hartman J. D., 2015, ApJ, 814, 35
Clements T. D., Henry T. J., Hosey A. D., Jao W.-C., Silverstein M. L., Winters J. G., Dieterich S. B., Riedel A. R., 2017, The Astronomical Journal, 154, 124
Davenport J. R. A., 2016, ApJ, 829, 23
Davenport J. R. A., et al., 2014, The Astrophysical Journal, 797, 122
Davenport J. R. A., Tovar Mendoza G., Hawley S. L., 2020, arXiv e-prints, p. arXiv:2005.10281
Doyle J. G., Butler C. J., van den Oord G. H. J., Kiang T., 1990, A&A, 232, 83
Dressing C. D., Charbonneau D., 2015, ApJ, 807, 45
Epstein C. R., Pinsonneault M. H., 2014, ApJ, 780, 159
Gaia Collaboration et al., 2018, A&A, 616, A1
Gershburg R. E., Shakahovskaya N. I., 1973, Nature Physical Science, 242, 85
Gizis J. E., Burgasser A. J., et al E. B., 2013, ApJ, 779, 172
Gizis J. E., Paudel R. R., Schmidt S. J., Williams P. K. G., Burgasser A. J., 2017, The Astrophysical Journal, 838, 22
Grootel V. V., et al., 2018, The Astrophysical Journal, 853, 30
Güdel M., 2004, A&ARv, 12, 71
Günther M. N., et al., 2020, AJ, 159, 60
Hannah I. G., Hudson H. S., Battaglia M., Christe S., Kašparová J., Krucker S., Kundu M. R., Veronig A., 2011, Space Sci. Rev., 159, 263
Hawley S. L., Pettersen B. R., 1991, ApJ, 378, 725
Hawley S. L., A. D. J. R., et al K. A. F., 2014b, ApJ, 797, 121
Hawley S. L., Davenport J. R. A., Kowalski A. F., Wisniewski J. P., Hebb L., Deitrick R., Hilton E. J., 2014a, ApJ, 797, 121
Henry James et al K., 2004, AJ, 128, 2460
Hilton E. J., 2011
Hilton E. J., West A. A., Hawley S. L., Kowalski A. F., 2010, AJ, 140, 1402
Holoien T. W.-S., S. B. J., et al S. K. Z., 2017, MNRAS, 467, 1098
Howell C. S., et al H. M., 2014, PASP, 126, 398
Hudson H. S., 1991, Sol. Phys., 133, 357
Hunt-Walker N. M., Hilton E. J., Kowalski A. F., Hawley S. L., Matthews J. M., 2012, PASP, 124, 545
Ilin E., Schmidt, Sarah J. Davenport, James R. A. Strassmeier, Klaus G. 2019, A&A, 622, A133
Khodachenko M. L., I R., et al L. H., 2007, AsBio, 7, 167
Kochanek C. S., J. S. B., et al S. K. Z., 2017, PASP, 129
Kowalski A. F., Hawley S., et al E. J. H., 2009, AJ, 138, 633
Kowalski L. H. S., et al W. J. P., 2013, ApJS, 207, 15
Lacy C. H., J M. T., S. E. D., 1976a, ApJS, 30, 85
Lacy C. H., Moffett T. J., Evans D. S., 1976b, ApJS, 30, 85
Lightkurve Collaboration et al., 2018, Lightkurve: Kepler and TESS time series analysis in Python, Astrophysics Source Code Library (ascl:1812.013)
Luger R., Barnes R., 2015, AsBio, 15, 119
Maehara H., T. S., et al N. S., 2012, Natur, 485, 478
Martínez R. R., Lopez L. A., Shappee B. J., Schmidt S. J., Jayasinghe T., Kochanek C. S., Auchettl K., Holoien T. W.-S., 2020, The Astrophysical Journal, 892, 144
McQuillan A., Aigrain S., Mazeh T., 2013, Monthly Notices of the Royal Astronomical Society, 432, 1203
Mondrik N., Newton E., Charbonneau D., Irwin J., 2018, The Astrophysical Journal, 870, 10
Notsu Y., et al., 2013, The Astrophysical Journal, 771, 127
Osten R. A., Wolk S. J., 2015, ApJ, 809, 79
Paudel R. R., Gizis J. E., Mullan D. J., Schmidt S. J., Burgasser A. J., Williams P. K. G., Berger E., 2018, The Astrophysical Journal, 858, 55
Paudel R. R., Gizis J. E., Mullan D. J., Schmidt S. J., Burgasser A. J., Williams P. K. G., Youngblood A., Stassun K. G., 2019, Monthly Notices of the Royal Astronomical Society, 486, 1438
Priest E. R., Forbes T. G., 2002, The Astronomy and Astrophysics Review, 10, 313
Raetz, St. Stelzer, B. Damasso, M. Scholz, A. 2020, A&A, 637, A22
Ricker G. R., et al., 2014, in Proc. SPIE. p. 914320 (arXiv:1406.0151), doi:10.1117/12.2063489
Saar S. H., Linsky J. L., 1985, in BAAS. p. 879
Schmidt S. J., L. P. J., et al S. K. Z., 2014, ApJL, 781, L24
Schmidt S. J., et al., 2019, The Astrophysical Journal, 876, 115
Segura A., M. W. L., andKasting J. M. V., S. H., 2010, AsBio, 10, 751
Shappee B. J., L. P. J., et al G. D., 2014, ApJ, 788, 48
Shields A. L., Ballard S., Johnson J. A., 2016, Phys. Rep., 663, 1
Silverberg S. M., F. K. A., et al D. J. R. A., 2016, ApJ, 829, 129
Simonian G., Z. S. K., et al S. S., 2016, ATel, 8803
Skumanich A., 1972, ApJ, 171, 565
Stanek K. Z., J. S. B., et al K. C. S., 2013, ATel, 5276
Tilley M. A., Segura A., Meadows V., Hawley S., Davenport J., 2019, Astrobiology, 19, 64
Virtanen P., et al., 2020, Nature Methods, 17, 261
West A. A., Hawley S. L., 2008, PASP, 120, 1161

This paper has been typeset from a TEX/LATEX file prepared by the author.